Optically Induced Three-Stage Picosecond Amorphization in Low-Temperature SrTiO₃

Thomas Linker, Subodh Tiwari, Shogo Fukushima, Rajiv K. Kalia, Aravind Krishnamoorthy, Aiichiro Nakano,* Ken-ichi Nomura, Kohei Shimamura, Fuyuki Shimojo, and Priya Vashishta

ACCESS | Metrics & More | Article Recommendations | Supporting Information

ABSTRACT: Photoexcitation can drastically modify potential energy surfaces of materials, allowing access to hidden phases. SrTiO₃ (STO) is an ideal material for photoexcitation studies due to its prevalent use in nanostructured devices and its rich range of functionality-changing lattice motions. Recently, a hidden ferroelectric phase in STO was accessed through weak terahertz excitation of polarization-inducing phonon modes. In contrast, whereas strong laser excitation was shown to induce nanostructures on STO surfaces and control nanopolarization patterns in STO-based heterostructures, the dynamic pathways underlying these optically induced structural changes remain unknown. Here nonadiabatic quantum molecular dynamics reveals picosecond amorphization in photoexcited STO at temperatures as low as 10 K. The three-stage pathway involves photoinduced charge transfer and optical phonon activation followed by nonlinear charge and lattice dynamics that ultimately lead to amorphization. This atomistic understanding could guide not only rational laser nanostructuring of STO but also broader "quantum materials on demand" technologies.
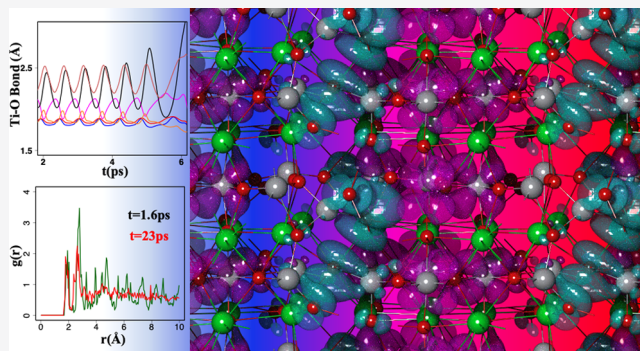
Strong laser excitation in materials can lead to nonequilibrium dynamics via carrier−phonon coupling[1−4] and charge transfer between atomic species.[5,6] The fast electron−ion dynamics involved in these processes can speed up access to different material phases typically obtained by thermal, straining, and other nonelectronic methods[7−9] or allow access to "hidden" nonequilibrium phases not obtainable by these means.[10] This has opened up a field of ultrafast science with the goal of obtaining desirable material properties on demand through experimental controls such as laser energy and fluence.[3,11,12] To create desirable functional materials by these methods, it is critical to understand the underlying electronic processes driving them.

An ideal material to study optically controlled material phases is SrTiO₃ (STO), as it not only has a wide variety of phase-change-inducing lattice motions, such as an antiferrodistortive (AFD) phase transition from the cubic to tetragonal structure below a critical temperature of $T_c \approx 105$ K and an optical phonon-mode-driven paraelectric-to-ferroelectric phase transition, but also is applied in numerous nanostructured devices.[13−17] Thus a fundamental understanding of photoexcited electron−lattice dynamics in STO will provide key insights into the optical control of a broad range of nanostructured devices. Recently, terahertz radiation was shown to induce a hidden metastable ferroelectric state in STO by directly coupling to optical phonon modes that induce spontaneous polarization in STO.[18,19] On the contrary, lattice

control of STO by above-band-gap optical excitation has been less explored, partly because it involves more subtle and intricate coupling between excited electrons and lattice motions via electronic-structure modification. Whereas femtosecond laser pulses have been shown to create nanostructures on STO surfaces[11,20] and modify nanopolarization patterns in ferroelectric/dielectric PbTiO₃/SrTiO₃ superlattices,[21] the microscopic mechanisms underlying this remarkable optical control remain elusive. The fundamental scientific question is, "What is the ultrafast pathway from electronic excitation to lattice change in STO upon optical excitation?"

Here we study the effects of strong electronic excitation on structural changes of STO in its low-temperature tetragonal phase using first-principles nonadiabatic quantum molecular dynamics (NAQMD) simulations; see the Methods. We find a photoinduced picosecond amorphization pathway that can occur at temperatures as low as 10 K. Detailed analyses reveal a three-stage mechanism due to coupled electron−lattice dynamics upon photoexcitation. Immediately after photo-
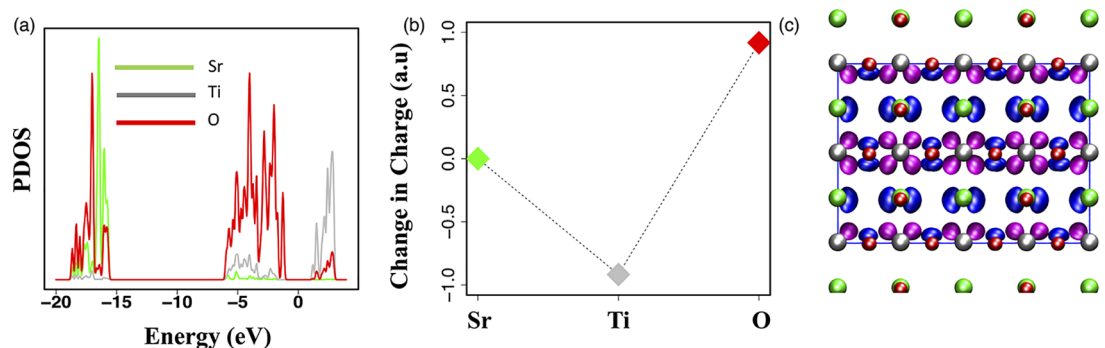
Figure 1. Initial excitation. (a) Atom-projected partial density of states (PDOS) in STO. The valence band maximum (VBM) is primarily composed of O states, whereas the conduction band minimum (CBM) is primarily composed of Ti states, indicating O-to-Ti charge transfer upon excitation. (b) Total change in charge of each atom type after excitation. (c) (010) projection of electron (magenta) and hole (blue) wave functions for excitation from VBM to CBM, where Sr, Ti, and O atoms are colored in green, gray, and red, respectively. As expected, the electron and hole wave functions are centered on Ti and O atoms, respectively.

excitation, we observe photoinduced charge transfer and coherent excitation of optical phonons via strong electron–phonon coupling. This is followed by nonlinear up-conversion, amplification and softening of phonons that cause unstable charge dynamics and electronic polarization accumulation. These charge-polarization dynamics ultimately lead to lattice destabilization and initiate an amorphization process dominated by Ti and O diffusion. Increasing temperature accelerates lattice disordering due to unstable electron–phonon dynamics, whereas large carrier concentrations rapidly destabilize the lattice, resulting in an ultrafast single-stage amorphization pathway as opposed to the three-stage pathway at smaller concentrations.

To study the effect of electronic excitation on the structural change of STO in its low-temperature tetragonal phase, we performed NAQMD simulations on a supercell composed of 2 × 2 × 1 tetragonal unit cells (in a total of 80 atoms). In each simulation, excitation is modeled as the instantaneous promotion of electrons from the valence band to the conduction band. To quantify the effects of the initial excitation, we first performed static density functional theory (DFT) calculations. We computed the atom-projected partial density of states (PDOS) to understand the expected charge transfer as a result of excitation. The PDOS in Figure 1a shows that electrons on the valence band edge are primarily localized around O atoms, whereas those on the conduction band edge are localized around Ti atoms. This implies charge transfer from O to Ti when optically excited.

We further corroborated this by computing the explicit charge transfer before and after excitation through Mulliken analysis.[22] Figure 1b shows the total change in atomic charge for each atom type corresponding to the excitation of an electron from the valence band maximum (VBM) to the conduction band minima (CBM). We see that O atoms become more positively charged, whereas Ti atoms become equally more negatively charged as a result of electron transfer from O to Ti atoms. On the contrary, the charge on Sr atoms remains the same after excitation, as their electronic states are deep within valence band. Figure 1c shows excited electron–hole wave functions corresponding to VBM-to-CBM excitation. The excited-electron wave function (magenta) is centered on Ti atoms, whereas the hole wave function (blue) is centered on O atoms. These results indicate that charge transfer between O and Ti will drive the dynamics resulting from electronic excitation.

After excitation, an NAQMD simulation was run at a temperature of 10 K in the canonical ensemble while allowing for phonon-assisted nonadiabatic transitions between electronic states (see Methods). Figure 2a–c shows the atomic motion, as described by the atomic mean-square displacement (MSD) divided into three distinct stages of motion. In the first stage of motion, the MSD in Figure 2a exhibits coherent low-frequency oscillations with a large amplitude as a result of excitation. Visual inspection indicates that the initial coherent motion has a period of ~0.5 ps. This is followed by a second stage marked by a drifting MSD with small higher frequency fluctuations, as illustrated by Figure 2b, which is indicative of phonon upconversion. After 6 ps, the MSD begins to increase, signifying the beginning of a third stage of motion. The third stage is marked by Ti and O diffusion (i.e., linear increase in MSD as a function of time), as illustrated in Figure 2c. The time-averaged radial distribution function (RDF) $g(r)$ is plotted for times centered at 1.62 and 23 ps after excitation in Figure 2d, where averaging was performed over 1 ps. Broadening of the second and higher peaks at 23 ps indicates structural disordering and the onset of amorphization. Further analysis via the examination of the partial RDFs is provided in Figure S1 in the Supporting Information (SI).

To further quantify the lattice dynamics, we plotted the time evolution of Ti–O and Sr–O bond lengths. Figure 2e–g shows all Ti–O bond lengths for a representative Ti atom in the three stages of motion, respectively. The colors in the figure correspond to individual bonds that are marked in Figure 2h. Similarly, Sr–O bond lengths for a representative Sr atom are shown in Figure 2i–k, and the corresponding colors are shown in Figure 2l. The Ti–O bond lengths and Sr–O bond lengths for all Ti and Sr atoms are plotted in Figures S2–S4. The initial low-frequency motion seen in the first stage of motion in the MSD can also be seen in the activation of coherent Ti–O and Sr–O bond oscillations, as illustrated in Figure 2e,i. In the second stage of motion, Figure 2f,j shows the amplification of Ti–O and Sr–O bond oscillations, which is indicative of phonon softening.[23] The large amplitudes of these phonon modes become ultimately unstable, leading to breaking of Ti–O and Sr–O bonds and chaotic bond dynamics, as illustrated in Figures 2g,k. To better understand the excited phonon dynamics, we computed the Fourier transform of the velocity autocorrelation function $D(\nu)$ during the first two stages of motion, shown in Figure 2m, and the Fourier transformation of average Ti–O and Sr–O bond
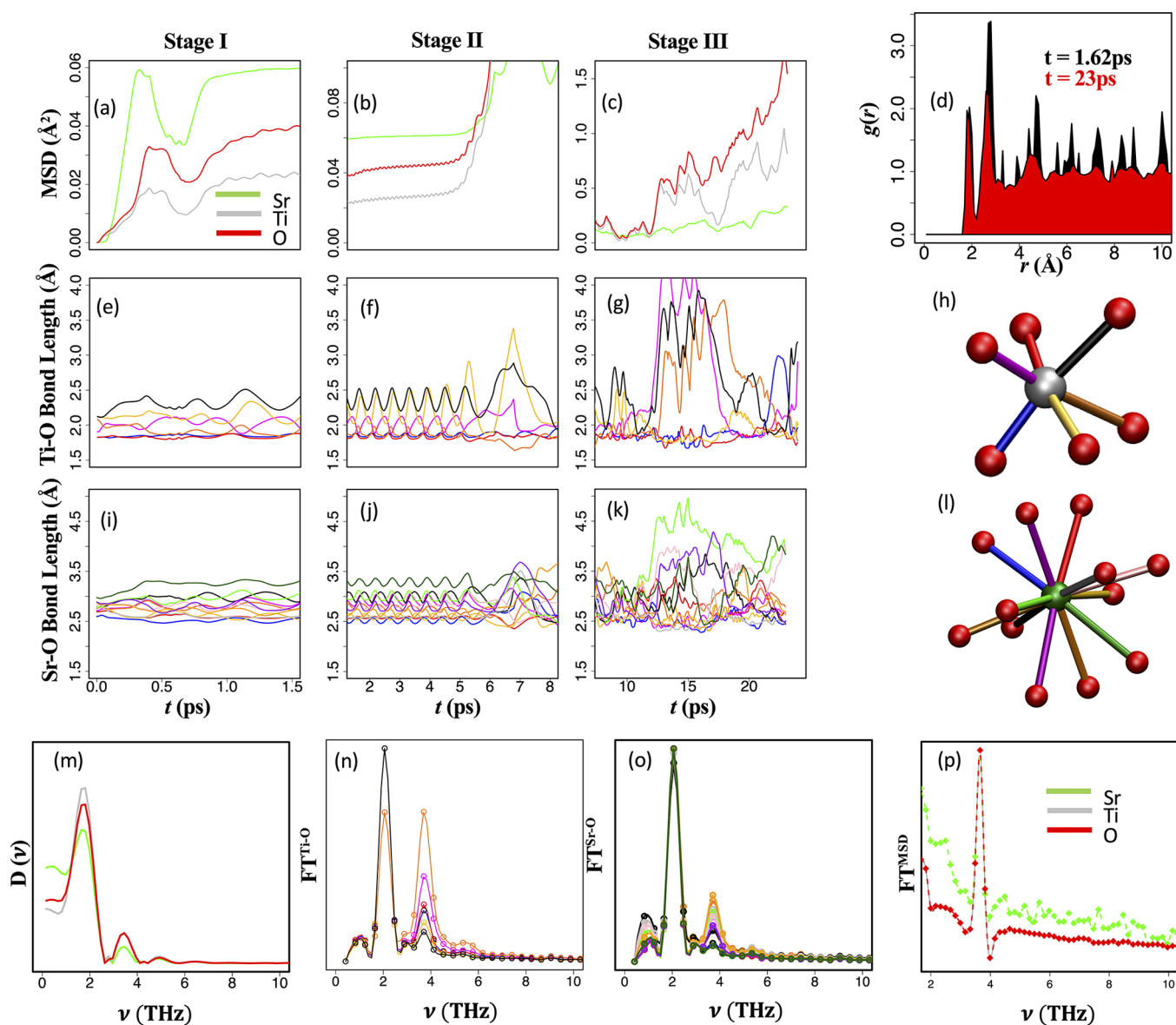
Figure 2. Lattice motion. (a−c) Atomic mean square displacement (MSD) for Sr (green), Ti (gray), and O (red) atoms divided into three stages of motion. Stage I is marked by the gradual activation of low-frequency phonons. Stage II is marked by a high-frequency MSD drift, indicating the activation of higher frequency phonon modes. Stage III is marked by lattice destabilization and amorphization driven by Ti and O diffusion. (d) Radial distribution function $g(r)$ at time $t = 1.62$ and 23 ps as it begins to amorphize. (e−g) Time evolution of Ti−O bond lengths for a given Ti atom divided into the three stages of motion, with specific Ti−O bonds colored in panel h. Similarly, panels i−k show the Sr−O bond evolution for a selected Sr atom with specific bonds colored in panel l. (m−p) Fourier transforms of the velocity autocorrelation function (m), average Ti−O bond lengths for each bond type (n), average Sr−O bond lengths for each bond-type (o), and MSD during Stage II of motion (p). These Fourier transforms indicate two dominant phonon frequencies, ~1.8 and ~3.8 THz.

fluctuations during the same period of motion, as shown in Figure 2n,o, respectively. All three Fourier transforms have distinct peaks at ~1.8 and ~3.8 THz. The 1.8 THz peak is consistent with the large coherent phonon activation seen in the initial stage of motion, whereas the 3.8 THz peak arises from the secondary phonon activation, that is, second harmonic generation.[24,25] We also plotted the Fourier transform of the MSD during the second stage of motion versus frequency ν in Figure 2p. For MSD, the frequency values were halved, as squaring doubles the frequency in the Fourier transform. The MSD thus plotted has a peak frequency of 3.8 THz (raw peak 7.6 THz), which further corroborates that this phonon mode is activated during the second stage of motion. The examination of atomic displacements upon

excitation indicates the initial activation of the ferroelectric (FE) A_{2u} mode upon excitation, which is consistent with the ~1.8 THz peak.[15,26] Video S1 shows the atomic displacements upon excitation. A diagram with marked A_{2u} mode displacements is also provided in Figure S5. The large-amplitude A_{2u} modes, in turn, result in nonlinear phonon coupling and upconversion to the secondary 3.8 THz peak seen in the second stage of motion, which we attribute to optical-branch O and Ti rotational modes about the c crystallographic axis. To highlight the secondary phonon activation of these rotational modes, Video S2 shows atomic displacements from the atomic configuration after 1.2 ps, so as to subtract out the initial displacement from A_{2u} mode activation. Video S3 shows
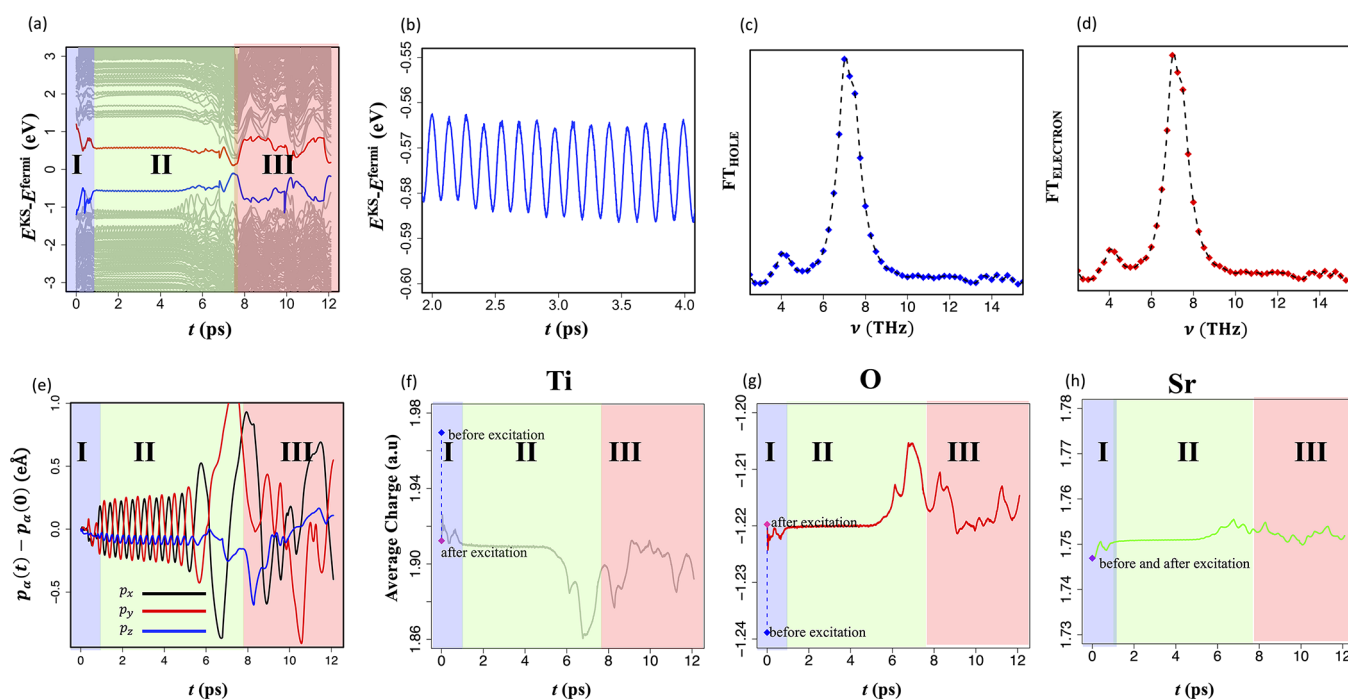
Figure 3. Electron−hole and charge dynamics. (a) Time evolution of Kohn−Sham (KS) eigenvalues from 0 to 12 ps divided into the three stages of lattice motion. (b) Zoom-in on the coherent evolution of the hole wave function during Stage II of lattice motion. (c,d) Fourier transforms of the hole and electron eigenenergy evolutions, respectively, during Stage II of motion. They both are characterized by a dominant high frequency of ∼7.5 THz. (e) Time evolution of the classical dipole moment, as defined in eq 1. The increasing oscillations of the classical dipole are indicative of an unstable polarization buildup during the coherent motion period. (f−h) Dynamics of the average charge for Ti, O, and Sr, respectively. There is an initial charge transfer from O−Ti as a result of excitation followed by a period of equilibration as the charge dynamics attempt to stabilize. The unstable polarization buildup ultimately destabilizes the charge dynamics, resulting in a large charge transfer from O−Ti as the lattice destabilizes.

atomic displacements for the entire trajectory, starting from 0 ps.

Recent studies have shown that weak THz excitation can specifically excite FE modes in STO, thereby creating a long-lasting metastable ferroelectric state.[18,19] This indicates that the energetics involved in transferring energy from excited carriers to the lattice, assisted by the transfer of charge between atomic species as a result of creating electron−hole pairs, ultimately causes these modes to become unstable.

To better understand the role of excited carriers and charge transfer in the unstable phonon dynamics, we plotted the time evolution of the Kohn−Sham (KS) eigenvalues, as illustrated in Figure 3a, with Stages I, II, and III labeled and highlighted with blue, green, and red background colors, respectively. Figure 3a demonstrates the relaxation of the excited electron (red curve) and hole (blue curve) during the first stage of motion, followed by coherent high-frequency motion in the second stage. Figure 3b shows the coherent hole evolution during the second stage. The Fourier transforms of both the hole and excited electron eigenenergy evolution during this period are shown in Figure 3c,d, respectively. Both the excited electron and hole states have dominant frequencies at 7.6 THz equal to approximately twice the frequency of the 3.8 THz mode seen in the Ti−O and Sr−O bond frequencies. Because the KS eigenenergy reflects the deviation of these bond lengths ($l(t)$) from their equilibrium values (l_{eq}), that is, $\delta l(t) = |l(t) - l_{eq}|$, its oscillation is characterized by two times the frequency of that of $l(t)$.[27] Thus this 7.6 THz peak is indicative of strong carrier−phonon coupling driving this phase of ionic motion.[3,27,28] As the lattice begins to destabilize after 6 ps, Figure 3a exhibits band-gap closing indicative of the reverse

Jahn−Teller effect.[29,30] After closing of the band gap, the excited carriers break free of their phonon-coupled state and become delocalized carriers that destabilize Ti−O and Sr−O bonds. Both the high-frequency coherent carrier motion and the free-carrier evolution resulting in bond destabilization are illustrated in Video S4.

To quantify the charge dynamics, we first computed a classical electron dipole moment, which is compliant with periodic boundary conditions (PBC)

$$p_\alpha(t) = e\frac{L_\alpha}{2\pi}\text{Im}\left(\log\left(\int_{V_{cell}} d^3r \; e^{i((2\pi r_\alpha)/L_\alpha)}\rho(\mathbf{r}, t)\right)\right) \tag{1}$$

where e is the electron charge, L_α is the length of αth Cartesian axis of the supercell ($\alpha = x$, y, or z), V_{cell} is the volume of the supercell, and $\rho(\mathbf{r}, t)$ is the excited-state electron charge density at spatial point $\mathbf{r} = (r_x, r_y, r_z)$ and time t. Figure 3e shows the time evolution of the change in the PBC-compliant electron dipole moment in all three Cartesian directions, with each stage of motion again labeled and highlighted with a different color. During the first stage of motion, there is little change in the electron PBC dipole moment upon excitation. In the second stage, as the unstable phonon modes begin to activate, a net asymmetrical change in the dipole moment forms with negatively averaged p_z oscillations and positively averaged p_x and p_y oscillations. The p_x and p_y oscillations slowly build up until they violently fluctuate as the lattice destabilizes. These building oscillations are indicative of unstable net electronic polarization accumulation as result of excitation, which leads to amorphization. The introduction of a spontaneous change in the electron-dipole moment along the [001] direction (i.e., c axis) is consistent with excitation of the
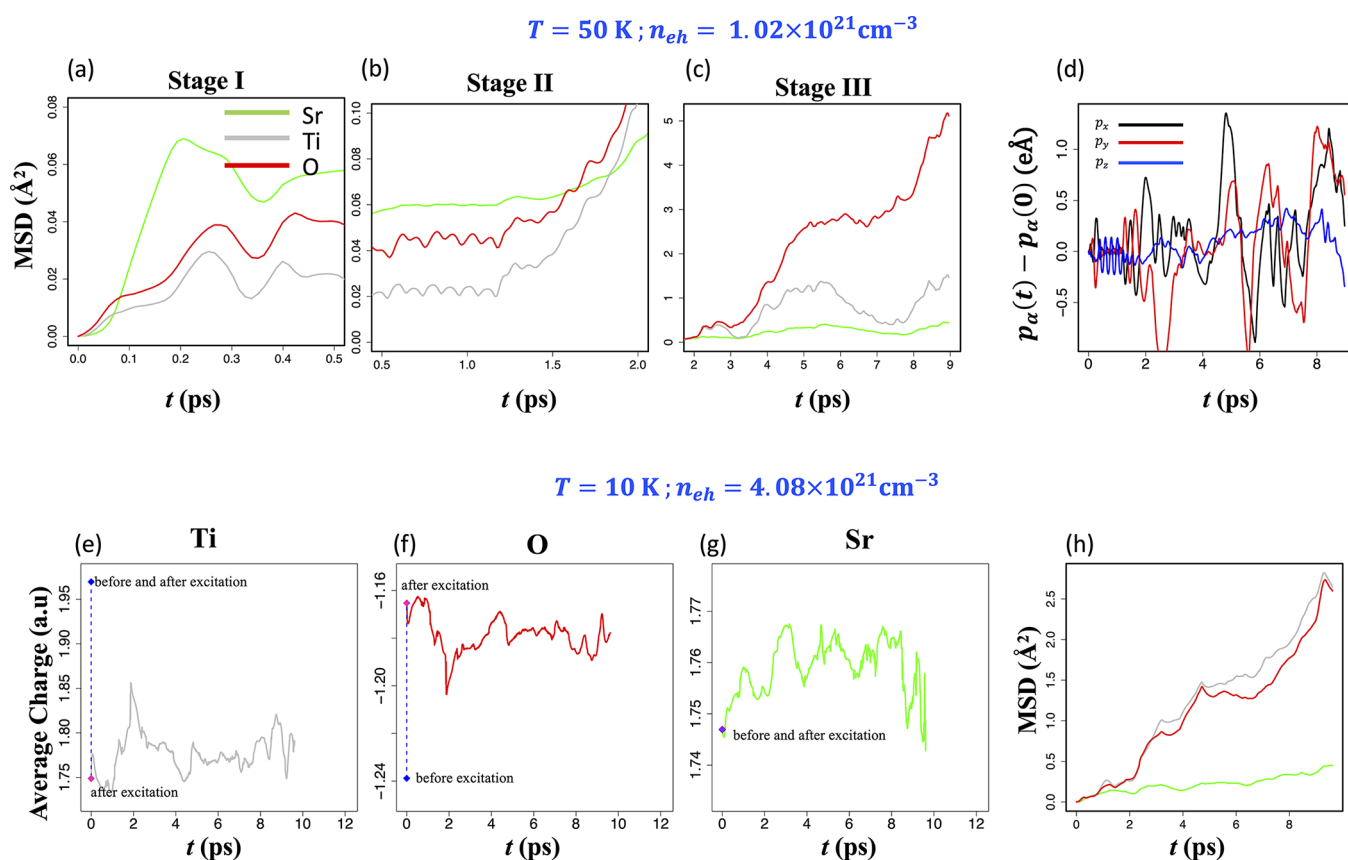
$$T = 50\,\mathrm{K}\,;n_{eh} = 1.02\times10^{21}\,\mathrm{cm}^{-3}$$

$$T = 10\,\mathrm{K}\,;n_{eh} = 4.08\times10^{21}\,\mathrm{cm}^{-3}$$

Figure 4. Effect of temperature and carrier concentration. (a−c) Atomic MSD at 50 K divided into three stages, as at 10 K, but the resonance period is now much shorter. (d) Time evolution of the classical PBC-compliant dipole moment. At 50 K, more phonon modes are activated, which leads to an earlier onset of violent fluctuations in the classical PBC-compliant dipole moment, leading to faster lattice destabilization. (e−g) Average charge dynamics for Ti, O, and Sr at 10 K with an increased carrier concentration. The increased carrier concentration leads to a large charge transfer from O−Ti, which immediately destabilizes the lattice, resulting in Ti and O diffusion, which is shown in panel h.

A_{2u} FE mode, indicating the source of the unstable oscillations in the dipole moment along the [100] and [010] directions to be strong carrier−phonon coupling to the 3.8 THz rotational modes. For comparison, the PBC-compliant total electronic moment for an adiabatic quantum molecular dynamics (QMD) trajectory at 10 K is plotted in Figure S6. We observed that the total electronic dipole moment remains constant, as no FE modes are present in the absence of electronic excitation. This confirms the electronic-excitation origin of the polarization dynamics in the NAQMD simulations. The efficacy of using eq 1 is discussed in the SI. An approximation of the total (ionic and electronic) polarization using the atomic Mulliken charge is also provided in Figure S7. A similar trend is seen with a change in the polarization along the c axis as a result of excitation of the A_{2u} FE mode.

We also examined the evolution of the average atomic charge of each atom type through Mulliken analysis, which is plotted in Figure 3f−h, with each stage of motion again labeled and highlighted with a different color. After the initial Ti−O charge transfer upon excitation in the first stage of motion, both the average Ti and O atomic charges tend to stabilize and form a new equilibrium. During the second stage of motion, the average Ti and O charge dynamics are quasistable, but an increase in the charge transfer from O−Ti begins to build as the lattice dynamics destabilize. The unstable electronic polarization builds up, ultimately resulting in a large charge transfer from O−Ti as the structure gets disordered. As the

amorphous structure sets in, the average O and Ti charge dynamics again tend to restabilize during the third stage of motion. Throughout the trajectory, the average charge on Sr is largely constant, as its electronic states are deep within the valence band, so that it is unaffected by the excited electron−hole dynamics.

To study the effect of carrier concentration and temperature, we ran the same MD simulations but with increased temperature and number of excited carriers. Figure 4a−c shows the ionic motion as described by the MSD, once again divided into three stages of motion for the MD trajectory at 50 K. Again, there are initially large atomic displacements during the first stage of motion, followed by a resonance period with higher frequency motion in the MSD into a final period of lattice destabilization and amorphization. The coherent-motion period is much shorter at 50 K due to increased phonon activation, which can be seen by multiple frequencies being present in the MSD in Figure 4b. This increased phonon activation at high temperature leads to an acceleration of the onset of violent fluctuations of the electron PBC-compliant dipole moment, as shown in Figure 4d.

Very large carrier concentrations, as illustrated in Figure 4e,f, can result in extreme charge transfer between O and Ti, which even causes large fluctuations in the average Sr charge, despite the fact that its electronic states lie deep within the valence band, as illustrated in Figure 4g. This large charge transfer quickly destabilizes the lattice, resulting in one-stage ultrafast amorphization dominated by Ti and O diffusion, as illustrated

in Figure 4h. Videos S5 and S6 show the atomic motion at 50 K and at 10 K with an increased carrier concentration, respectively.

We have performed NAQMD simulations on STO and found that strong optical excitation can result in coherent phonon activation that leads to unstable phonon and charge dynamics, ultimately resulting in lattice destabilization and amorphization. In particular, we find the excitation of the ferroelectric A_{2u} mode, indicating that a weaker laser fluence could provide a possible alternative path to the ferroelectric phase transition other than terahertz excitation if the effects of the strong carrier–phonon coupling can be mitigated. Judicious doping could also mitigate these effects by limiting the charge transfer from O to Ti that results in bond destabilization.

Furthermore, amorphous STO has significantly different functional properties from those of its crystalline paraelectric counterpart, and laser excitation may allow ultrafast access to those distinct properties. For example, nanometer-thick films of amorphous STO have been shown to have unique piezoelectric and pyroelectric phases.[31,32] Combined with the strong optical excitation-induced transition to an amorphous structure found in this Letter, this indicates potential access to a piezo/pyro-electric phase transition by laser pulses. Such ultrafast access to a piezo/pyro-electric phase transition will complement the hidden paraelectric–ferroelectric phase transition via the weak optical excitation previously mentioned, thereby offering laser control over a "full stack" of STO electrical properties. Our results thus promote STO as a strong candidate material for much richer optical functional control than was previously known, warranting further experimental study via ultrafast measurements.

METHODS

To study the effect of optical excitation on STO, we preformed NAQMD simulations. QMD[33,34] is an *ab initio* method that integrates the trajectories of all atoms by computing their interatomic forces from first-principles in the framework of DFT.[35] DFT calculations were performed using a plane-wave basis with Vanderbilt-style ultrasoft pseudopotentials[36] (USPPs), and the local-spin density approximation was used to approximate the exchange correlation functional.[37] A plane-wave cutoff energy of 30 Ry was used for electronic wave functions, and 250 Ry was used for the electronic charge density. NAQMD[38−42] allows for dynamics of excited carriers to be modeled within the framework of time-dependent DFT (TDDFT),[43] with ionic-motion-assisted transitions between electronic states modeled using the fewest-switch surface-hopping approach.[41,44] Details of our NAQMD simulation method for photoexcited electron–ion dynamics can be found in ref 39.

Our simulations were performed on a supercell of $2 \times 2 \times 1$ tetragonal STO crystalline unit cells containing a total of 80 atoms with lattice constants of $a = b = 5.56$ Å and $c = 7.90$ Å. NAQMD simulations were performed in a canonical ensemble at temperatures of 10 and 50 K using a Nosé–Hoover thermostat.[45] A time step of 1.206 fs was used, and the gamma point was used to sample the Brillouin zone. The NAQMD algorithm was implemented in the highly parallelized plane-wave basis quantum molecular dynamics simulation code QXMD.[46]

ASSOCIATED CONTENT

ⓈⒾ Supporting Information

The Supporting Information is available free of charge at https://pubs.acs.org/doi/10.1021/acs.jpclett.0c02873.

> Figure S1. Partial RDFs. Figure S2. Time evolution of Ti−O bond lengths for all 16 Ti atoms at 10 K. Figure S3. Time evolution of Sr−O bond lengths for all 16 Sr atoms. Figure S4. Ti−O and Sr−O bonds. Figure S5. A_{2u} phonon displacements. Figure S6. Classical PBC-compliant dipole moment for excited NAQMD and ground-state QMD trajectories. Figure S7. Polarization calculation using Mulliken charge (PDF)
>
> Supplemental videos of atomic displacements and electron-hole motion (ZIP)

AUTHOR INFORMATION

Corresponding Author

Aiichiro Nakano − *Collaboratory for Advanced Computing and Simulations, University of Southern California, Los Angeles, California 90089-0242, United States;* ⓘ orcid.org/0000-0003-3228-3896; Email: anakano@usc.edu

Authors

Thomas Linker − *Collaboratory for Advanced Computing and Simulations, University of Southern California, Los Angeles, California 90089-0242, United States*

Subodh Tiwari − *Collaboratory for Advanced Computing and Simulations, University of Southern California, Los Angeles, California 90089-0242, United States;* ⓘ orcid.org/0000-0002-5516-6900

Shogo Fukushima − *Department of Physics, Kumamoto University, Kumamoto 860-8555, Japan*

Rajiv K. Kalia − *Collaboratory for Advanced Computing and Simulations, University of Southern California, Los Angeles, California 90089-0242, United States*

Aravind Krishnamoorthy − *Collaboratory for Advanced Computing and Simulations, University of Southern California, Los Angeles, California 90089-0242, United States;* ⓘ orcid.org/0000-0001-6778-2471

Ken-ichi Nomura − *Collaboratory for Advanced Computing and Simulations, University of Southern California, Los Angeles, California 90089-0242, United States*

Kohei Shimamura − *Department of Physics, Kumamoto University, Kumamoto 860-8555, Japan;* ⓘ orcid.org/0000-0003-3235-2599

Fuyuki Shimojo − *Department of Physics, Kumamoto University, Kumamoto 860-8555, Japan*

Priya Vashishta − *Collaboratory for Advanced Computing and Simulations, University of Southern California, Los Angeles, California 90089-0242, United States;* ⓘ orcid.org/0000-0003-4683-429X

Complete contact information is available at:
https://pubs.acs.org/10.1021/acs.jpclett.0c02873

Author Contributions

T.L. performed the nonadiabatic quantum molecular dynamics simulation. T.L. and S.T. performed the analysis of the simulation. R.K.K., A.K., A.N., K.-i.N, K.S, F.S., and P.V. designed the research. All authors participated in the analysis of the data and writing of the manuscript

Notes

The authors declare no competing financial interest.

ACKNOWLEDGMENTS

REFERENCES

(1) Bang, J.; Meng, S.; Sun, Y.-Y.; West, D.; Wang, Z.; Gao, F.; Zhang, S. B. Regulating Energy Transfer of Excited Carriers and the Case for Excitation-Induced Hydrogen Dissociation on Hydrogenated Graphene. *Proc. Natl. Acad. Sci. U. S. A.* **2013**, *110* (3), 908−911.

(2) Lisowski, M.; Loukakos, P. A.; Bovensiepen, U.; Stähler, J.; Gahl, C.; Wolf, M. Ultra-Fast Dynamics of Electron Thermalization, Cooling and Transport Effects in Ru(001). *Appl. Phys. A: Mater. Sci. Process.* **2004**, *78* (2), 165−176.

(3) Krishnamoorthy, A.; Lin, M.-F.; Zhang, X.; Weninger, C.; Ma, R.; Britz, A.; Tiwary, C. S.; Kochat, V.; Apte, A.; Yang, J.; Park, S.; Li, R.; Shen, X.; Wang, X.; Kalia, R.; Nakano, A.; Shimojo, F.; Fritz, D.; Bergmann, U.; Ajayan, P.; Vashishta, P. Optical Control of Non-Equilibrium Phonon Dynamics. *Nano Lett.* **2019**, *19* (8), 4981−4989.

(4) Bassman, L.; Krishnamoorthy, A.; Kumazoe, H.; Misawa, M.; Shimojo, F.; Kalia, R. K.; Nakano, A.; Vashishta, P. Electronic Origin of Optically-Induced Sub-Picosecond Lattice Dynamics in $MoSe_2$ Monolayer. *Nano Lett.* **2018**, *18* (8), 4653−4658.

(5) Hong, X.; Kim, J.; Shi, S.-F.; Zhang, Y.; Jin, C.; Sun, Y.; Tongay, S.; Wu, J.; Zhang, Y.; Wang, F. Ultrafast Charge Transfer in Atomically Thin MoS_2/WS_2 Heterostructures. *Nat. Nanotechnol.* **2014**, *9* (9), 682−686.

(6) Porer, M.; Fechner, M.; Kubli, M.; Neugebauer, M. J.; Parchenko, S.; Esposito, V.; Narayan, A.; Spaldin, N. A.; Huber, R.; Radovic, M.; Bothschafter, E. M.; Glownia, J. M.; Sato, T.; Song, S.; Johnson, S. L.; Staub, U. Ultrafast Transient Increase of Oxygen Octahedral Rotations in a Perovskite. *Phys. Rev. Res.* **2019**, *1* (1), 12005.

(7) Rousse, A.; Rischel, C.; Fourmaux, S.; Uschmann, I.; Sebban, S.; Grillon, G.; Balcou, P.; Förster, E.; Geindre, J. P.; Audebert, P.; Gauthier, J. C.; Hulin, D. Non-Thermal Melting in Semiconductors Measured at Femtosecond Resolution. *Nature* **2001**, *410* (6824), 65−68.

(8) Tavella, F.; Höppner, H.; Tkachenko, V.; Medvedev, N.; Capotondi, F.; Golz, T.; Kai, Y.; Manfredda, M.; Pedersoli, E.; Prandolini, M. J.; Stojanovic, N.; Tanikawa, T.; Teubner, U.; Toleikis, S.; Ziaja, B. Soft X-Ray Induced Femtosecond Solid-to-Solid Phase Transition. *High Energy Density Phys.* **2017**, *24*, 22−27.

(9) Lee, C.; Yan, H.; Brus, L. E.; Heinz, T. F.; Hone, J.; Ryu, S. Anomalous Lattice Vibrations of Single- and Few-Layer MoS_2. *ACS Nano* **2010**, *4* (5), 2695−2700.

(10) Stojchevska, L.; Vaskivskyi, I.; Mertelj, T.; Kusar, P.; Svetin, D.; Brazovskii, S.; Mihailovic, D. Ultrafast Switching to a Stable Hidden Quantum State in an Electronic Crystal. *Science* **2014**, *344* (6180), 177−180.

(11) Deng, G.; Xiao, Y.; Yang, M.; Zhou, H.; Yang, H.; Feng, G.; Zhou, S. Femtosecond Laser Induced Surface Nanostructures on $SrTiO_3$. *Laser Phys. Lett.* **2019**, *16* (5), No. 056007.

(12) Stern, M. J.; René de Cotret, L. P.; Otto, M. R.; Chatelain, R. P.; Boisvert, J.-P.; Sutton, M.; Siwick, B. J. Mapping Momentum-Dependent Electron-Phonon Coupling and Nonequilibrium Phonon Dynamics with Ultrafast Electron Diffuse Scattering. *Phys. Rev. B: Condens. Matter Mater. Phys.* **2018**, *97* (16), 165416.

(13) Padilla, J.; Vanderbilt, D. Ab Initio Study of $SrTiO_3$ Surfaces. *Surf. Sci.* **1998**, *418* (1), 64−70.

(14) Pai, Y. Y.; Tylan-Tyler, A.; Irvin, P.; Levy, J. Physics of $SrTiO_3$-Based Heterostructures and Nanostructures: A Review. *Rep. Prog. Phys.* **2018**, *81*, No. 036503.

(15) Evarestov, R. A.; Blokhin, E.; Gryaznov, D.; Kotomin, E. A.; Maier, J. Phonon Calculations in Cubic and Tetragonal Phases of $SrTiO_3$: A Comparative LCAO and Plane-Wave Study. *Phys. Rev. B: Condens. Matter Mater. Phys.* **2011**, *83* (13), 1−9.

(16) Marrocchelli, D.; Sun, L.; Yildiz, B. Dislocations in $SrTiO_3$: Easy To Reduce but Not so Fast for Oxygen Transport. *J. Am. Chem. Soc.* **2015**, *137* (14), 4735−4748.

(17) Liu, P.; Nisar, J.; Pathak, B.; Ahuja, R. Hybrid Density Functional Study on $SrTiO_3$ for Visible Light Photocatalysis. *Int. J. Hydrogen Energy* **2012**, *37* (16), 11611−11617.

(18) Li, X.; Qiu, T.; Zhang, J.; Baldini, E.; Lu, J.; Rappe, A. M.; Nelson, K. A. Terahertz Field−Induced Ferroelectricity in Quantum Paraelectric $SrTiO_3$. *Science* **2019**, *364* (6445), 1079−1082.

(19) Kozina, M.; Fechner, M.; Marsik, P.; van Driel, T.; Glownia, J. M.; Bernhard, C.; Radovic, M.; Zhu, D.; Bonetti, S.; Staub, U.; Hoffmann, M. C. Terahertz-Driven Phonon Upconversion in $SrTiO_3$. *Nat. Phys.* **2019**, *15* (4), 387−392.

(20) Song, J.; Wang, X.; Hu, X.; Xu, J.; Liao, Y.; Sun, H.; Qiu, J.; Xu, Z. Orientation-Controllable Self-Organized Microgratings Induced in the Bulk $SrTiO_3$ Crystal by a Single Femtosecond Laser Beam. *Opt. Express* **2007**, *15* (22), 14524.

(21) Stoica, V. A.; Laanait, N.; Dai, C.; Hong, Z.; Yuan, Y.; Zhang, Z.; Lei, S.; McCarter, M. R.; Yadav, A.; Damodaran, A. R.; Das, S.; Stone, G. A.; Karapetrova, J.; Walko, D. A.; Zhang, X.; Martin, L. W.; Ramesh, R.; Chen, L. Q.; Wen, H.; Gopalan, V.; Freeland, J. W. Optical Creation of a Supercrystal with Three-Dimensional Nanoscale Periodicity. *Nat. Mater.* **2019**, *18* (4), 377−383.

(22) Mulliken, R. S. Electronic Population Analysis on LCAO−MO Molecular Wave Functions. I. *J. Chem. Phys.* **1955**, *23* (10), 1833−1840.

(23) Park, H. J.; Sohn, C. H.; Jeong, D. W.; Cao, G.; Kim, K. W.; Moon, S. J.; Jin, H.; Cho, D.-Y.; Noh, T. W. Phonon-Assisted Optical Excitation in the Narrow Bandgap Mott Insulator $Sr_3Ir_2O_7$. *Phys. Rev. B: Condens. Matter Mater. Phys.* **2014**, *89* (15), 155115.

(24) Miller, R. C. Optical Second Harmonic Generation In Piezoelectric Crystals. *Appl. Phys. Lett.* **1964**, *5* (1), 17−19.

(25) Li, Z.; Jin, Y.-Q.; Tohyama, T.; Iitaka, T.; Zhang, J.-X.; Su, H. Second Harmonic Generation in the Weyl Semimetal TaAs from a Quantum Kinetic Equation. *Phys. Rev. B: Condens. Matter Mater. Phys.* **2018**, *97* (8), 85201.

(26) Trautmann, T.; Falter, C. Lattice Dynamics, Dielectric Properties and Structural Instabilities of $SrTiO_3$ and $BaTiO_3$. In. *J. Phys.: Condens. Matter* **2004**, *16*, 5955−5977.

(27) Mou, W.; Ohmura, S.; Shimojo, F.; Nakano, A. Molecular Control of Photoexcited Charge Transfer and Recombination at a Quaterthiophene/Zinc Oxide Interface. *Appl. Phys. Lett.* **2012**, *100* (20), 203306.

(28) Linker, T. M.; Tiwari, S.; Kumazoe, H.; Fukushima, S.; Kalia, R. K.; Nakano, A.; Ramprasad, R.; Shimojo, F.; Vashishta, P. Field-Induced Carrier Localization Transition in Dielectric Polymers. *J. Phys. Chem. Lett.* **2020**, *11* (2), 352−358.

(29) Gilman, J. J. During Detonation Chemistry May Precede Heat. *Mater. Sci. Technol.* **2006**, *22* (4), 430−437.

(30) Shimamura, K.; Misawa, M.; Li, Y.; Kalia, R. K.; Nakano, A.; Shimojo, F.; Vashishta, P. A Crossover in Anisotropic Nano-mechanochemistry of van Der Waals Crystals. *Appl. Phys. Lett.* **2015**, *107* (23), 231903.

(31) Ehre, D.; Lyahovitskaya, V.; Tagantsev, A.; Lubomirsky, I. Amorphous Piezo- and Pyroelectric Phases of $BaZrO_3$ and $SrTiO_3$. *Adv. Mater.* **2007**, *19* (11), 1515−1517.

(32) Frenkel, A. I.; Ehre, D.; Lyahovitskaya, V.; Kanner, L.; Wachtel, E.; Lubomirsky, I. Origin of Polarity in Amorphous $SrTiO_3$. *Phys. Rev. Lett.* **2007**, *99* (21), 10−13.

(33) Car, R.; Parrinello, M. Unified Approach for Molecular Dynamics and Density-Functional Theory. *Phys. Rev. Lett.* **1985**, *55* (22), 2471−2474.

(34) Payne, M. C.; Teter, M. P.; Allan, D. C.; Arias, T. A.; Joannopoulos, J. D. Iterative Minimization Techniques for Ab Initio Total-Energy Calculations: Molecular Dynamics and Conjugate Gradients. *Rev. Mod. Phys.* **1992**, *64* (4), 1045−1097.

(35) Kohn, W.; Sham, L. J. Self-Consistent Equations Including Exchange and Correlation Effects. *Phys. Rev.* **1965**, *140* (4A), A1133−A1138.

(36) Laasonen, K.; Pasquarello, A.; Car, R.; Lee, C.; Vanderbilt, D. Car-Parrinello Molecular Dynamics with Vanderbilt Ultrasoft Pseudopotentials. *Phys. Rev. B: Condens. Matter Mater. Phys.* **1993**, *47* (16), 10142−10153.

(37) Gunnarsson, O.; Lundqvist, B. I. Exchange and Correlation in Atoms, Molecules, and Solids by the Spin-Density-Functional Formalism. *Phys. Rev. B* **1976**, *13* (10), 4274−4298.

(38) Shimojo, F.; Ohmura, S.; Mou, W.; Kalia, R. K.; Nakano, A.; Vashishta, P. Large Nonadiabatic Quantum Molecular Dynamics Simulations on Parallel Computers. *Comput. Phys. Commun.* **2013**, *184* (1), 1−8.

(39) Shimojo, F.; Hattori, S.; Kalia, R. K.; Kunaseth, M.; Mou, W.; Nakano, A.; Nomura, K. I.; Ohmura, S.; Rajak, P.; Shimamura, K.; Vashishta, P. A Divide-Conquer-Recombine Algorithmic Paradigm for Large Spatiotemporal Quantum Molecular Dynamics Simulations. *J. Chem. Phys.* **2014**, *140* (18), 18A529.

(40) Imachi, H.; Yokoyama, S.; Kaji, T.; Abe, Y.; Tada, T.; Hoshi, T. One-Hundred-Nm-Scale Electronic Structure and Transport Calculations of Organic Polymers on the K Computer. *AIP Conf. Proc.* **2016**, *1790* (1), 020010.

(41) Craig, C. F.; Duncan, W. R.; Prezhdo, O. V. Trajectory Surface Hopping in the Time-Dependent Kohn-Sham Approach for Electron-Nuclear Dynamics. *Phys. Rev. Lett.* **2005**, *95* (16), 163001.

(42) Meng, S.; Kaxiras, E. Real-Time, Local Basis-Set Implementation of Time-Dependent Density Functional Theory for Excited State Dynamics Simulations. *J. Chem. Phys.* **2008**, *129* (5), 054110.

(43) Runge, E.; Gross, E. K. U. Density-Functional Theory for Time-Dependent Systems. *Phys. Rev. Lett.* **1984**, *52* (12), 997−1000.

(44) Tully, J. C. Molecular Dynamics with Electronic Transitions. *J. Chem. Phys.* **1990**, *93* (2), 1061−1071.

(45) Nosé, S. A Molecular Dynamics Method for Simulations in the Canonical Ensemble. *Mol. Phys.* **1984**, *52* (2), 255−268.

(46) Shimojo, F.; Fukushima, S.; Kumazoe, H.; Misawa, M.; Ohmura, S.; Rajak, P.; Shimamura, K.; Bassman, L.; Tiwari, S.; Kalia, R. K.; Nakano, A.; Vashishta, P. QXMD: An Open-Source Program for Nonadiabatic Quantum Molecular Dynamics. *SoftwareX* **2019**, *10*, 100307.